Room-Temperature Single-Electron Charging Detected by Electrostatic Force Microscopy

Antoni Tekiel,* Yoichi Miyahara, Jessica M. Topple, and Peter Grutter

Physics Department, McGill University, 3600 University Street, Montreal, QC H3A 2T8, Canada

ABSTRACT We use atomic force microscopy to measure electron addition spectra of individual Au nanoparticles that exhibit Coulomb blockade at room temperature. The cantilever tip charges individual nanoparticles supported on an ultra-thin NaCl film *via* single-electron tunneling from the metal back electrode. The tunneling is detected by measuring frequency shift and damping of the oscillating cantilever. Finite element electrostatic calculations indicate that the total nanoparticle capacitance is dominated by mutual capacitance to the back electrode.

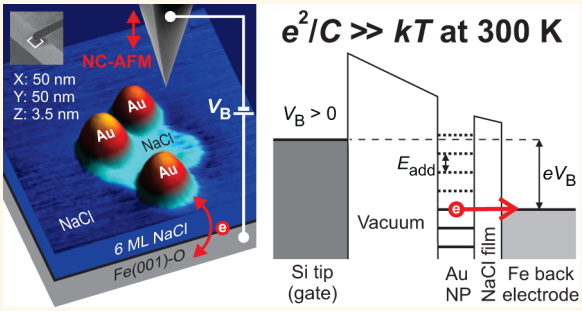

KEYWORDS: Coulomb blockade · capacitance · single-electron tunneling · room-temperature charge stability · Au nanoparticles · atomic force microscopy · finite element method

In nanoelectronic devices where components are connected by tunnel barriers and capacitively coupled to external electrodes, the transport can be dominated by single electron effects. Among such phenomena, Coulomb charging plays a key role in many systems, including single electron transistors and single electron memory devices. Measurement of the capacitance between the components of nanoscale circuits and understanding its origin is of great importance for the effort of improving such devices in order to work reliably at room temperature.[1,2] However, characterization of local electronic properties becomes increasingly challenging as structures are reduced to nanoscale dimensions. Methods based on transport measurements and conventional charge sensing are limited in flexibility since they require lithographic techniques to fabricate nanoscale electrodes. In this work, we use electrostatic force microscopy with single-electron sensitivity (*e*-EFM) to characterize charging of individual Au nanoparticles (NP), including measurement of electron addition spectra and tunneling rates. The nanoparticles are separated from an Fe(001) back electrode by an ultra-thin NaCl film and due to their small size exhibit Coulomb blockade at room temperature. Because the *e*-EFM technique can both image the topography of the studied device and measure electronic properties of individual nanoparticles, it allows for exploring structure–property relationships. Given the simple design of the studied system, we use finite element electrostatic simulation to examine the relevant contributions to the total nanoparticle capacitance, which is determined experimentally from the measurement of electron addition energy. The results point toward a total capacitance dominated by the mutual capacitance between the nanoparticle and the back electrode. A comparison of the experimentally determined capacitance with numerical simulations indicates that the nanoparticles should be modeled as truncated spheres in order to reduce the mutual capacitance to the substrate.

The *e*-EFM technique is a new and extremely versatile method that is based on noncontact atomic force microscopy (NC-AFM) and suited for characterization of nanostructures supported on thin insulating films. In *e*-EFM an oscillating AFM tip is used both as a gate to charge individual nanoparticles with single electrons from a conducting back electrode, and a charge-sensitive probe to detect the tunneling through a change in cantilever energy dissipation. As a scanning

* Address correspondence to antoni.tekiel@mail.mcgill.ca.

Received for review April 14, 2013 and accepted May 2, 2013.

Published online May 02, 2013
10.1021/nn401840n

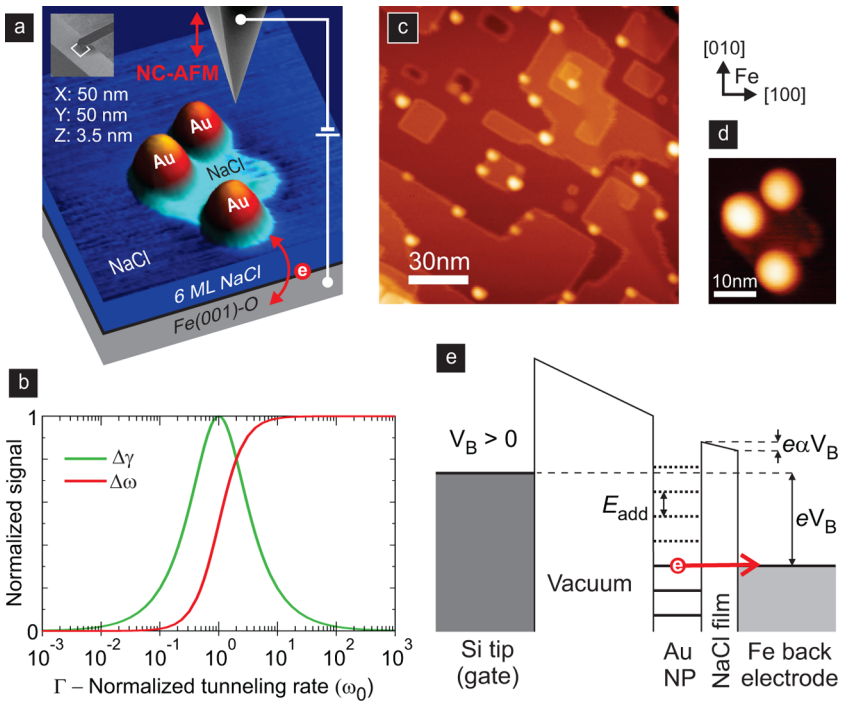

Figure 1. (a) Schematic of the studied system. The AFM tip is used as a local gate to charge individual nanoparticles with electrons from the back electrode. (b) Plot of the dissipation and resonance frequency shift response (in normalized units) *versus* the normalized tunneling rate (in units of the cantilever resonance frequency, $\omega_0 = 2\pi f_0$). (c) Topography of an NaCl thin film with a submonolayer coverage of Au that self-assembled into homogeneous nanoparticles. (d) Topography of studied Au nanoparticles (the width of the nanoparticles derived from AFM measurements is overestimated). (e) Energy diagram of the system for positive sample bias allowing for sequential unloading of electrons.

probe technique, *e*-EFM can routinely access nanometer length scale and offers an alternative approach that overcomes the difficulty in attaching the electrodes. The *e*-EFM technique has been successfully used at cryogenic temperatures[3−9] to measure energy spectra (ground[8] and excited states[9]), electron tunneling rates, as well as shell structures[8] of various nanoscale structures and entities. It is clear that in principle this technique, which has been used at temperatures as high as 95 K,[8] could also work at room temperature and lead to wide-ranging applications.[6] So far, however, the only *e*-EFM experiment conducted at room temperature reported a relatively weak signal,[10] making characterization of individual nanostructures difficult. In this work, we extend the *e*-EFM technique to room temperature by carefully tuning the sample design and fabrication relative to the cantilever response to achieve maximum sensitivity.

The essential part of the *e*-EFM method is an insulating film that separates the nanostructures under investigation from a back electrode, which is shown schematically in Figure 1a. The rate of tunneling through the thin insulating film largely decides the sensitivity of the method by affecting the relative strength of the cantilever dissipation and frequency shift signals,[6] which are measured in *e*-EFM. Figure 1b shows that the dissipation of the cantilever, $\Delta\gamma$, is maximal when the tunneling rate is matched with the oscillation frequency of the cantilever, while the frequency shift, $\Delta\omega = 2\pi\Delta f$, increases with increasing tunneling rate (see also the Supporting Information). Although the signal could be optimized by a proper choice of the cantilever, this imposes a potential limitation due to the range of resonance frequencies (10−1000 kHz) of commercially available AFM probes. Alternatively, the *e*-EFM technique can be made sensitive at room temperature by achieving full control over the tunnel barrier thickness and adjusting the tunneling rate to the cantilever resonance frequency. We utilize an ultra-thin epitaxial NaCl film as the tunnel barrier, grown under ultra-high vacuum (UHV) on the Fe(001)-p(1 × 1)O surface of the Fe back electrode. Our group has recently developed a method to grow such films layer by layer with a small number of defects.[11] Metal nanoparticles, formed by thermally evaporating Au onto the NaCl surface, are used as electron confining nanostructures.

RESULTS AND DISCUSSION

Figure 1c shows an NaCl film at a nominal thickness of 7 atomic monolayers (ML) with a submonolayer coverage of Au. The epitaxial NaCl film has a (001) orientation and a (4 × 4) symmetry with charge-neutral step edges oriented along the ⟨110⟩ directions of the Fe(001) substrate. It grows in a near perfect layer-by-layer mode, allowing for precise control of the tunnel barrier thickness.[11] Although the underlying step edges of Fe slightly disturb the nearby growth of NaCl, on flat

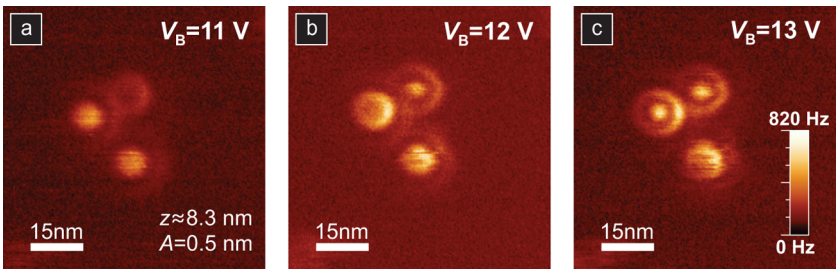

Figure 2. Dissipation (γ) images taken at room temperature showing the same three Au nanoparticles as Figure 1d, tip height $z \approx 8.3$ nm and cantilever oscillation amplitude $A = 0.5$ nm. The bias voltage across the tunnel barrier, equal to $\alpha(x,y,z)V_B$, was gradually increased by changing V_B from 11 to 13 V, allowing for tunneling of a larger number of electrons.

substrate areas the film is characterized by an almost complete sixth ML, and a far from complete seventh ML. On the NaCl film, as shown in Figure 1c, Au reveals a strong affinity for substrate steps, similarly to alkali halide bulk surfaces,[12−15] To meet the requirement for the electron addition energy, E_{add}, to be larger than k_BT at room temperature, a small amount of Au (approximately 0.02 ML) was deposited that resulted in a formation of isolated nanoparticles (with an average number density of 1.3×10^{11} NP/cm^2). The nanoparticles are anchored symmetrically above NaCl step edges and are homogeneous in size. In Figure 1d, the size of the studied nanoparticles is characterized by a height of 3.5 nm when measured from the lower NaCl terrace and a diameter of approximately 10 nm. In topography characterization, the AFM tip usually leads to increased lateral dimensions due to tip convolution effects.[12,13,15] For this reason, the width of the nanoparticles derived from the AFM topography measurement is certainly overestimated.

To induce tunneling between a supported Au nanoparticle and the back electrode, the AFM tip is placed within several nanometers above the nanoparticle (see Figure 1a). A DC bias voltage, V_B, is applied to the back electrode, while the oscillating cantilever is electrically grounded. Tunneling between the tip and the nanoparticle is negligible because of the large barrier height and width (∼5 nm) of the vacuum gap. The potential drop between the Au nanoparticle and the back electrode, *i.e.*, across the NaCl tunnel barrier, is a fraction of the applied bias voltage, αV_B ($\alpha < 1$). The $\alpha(x,y,z)$ parameter (commonly called the lever-arm) depends on the lateral and vertical position of the tip. Consequently, even small tip oscillations modulate α, leading to an effective modulation of the voltage across the barrier. Tunneling of an electron between the back electrode and the Au nanoparticle only takes place if the Coulomb blockade is lifted by selecting a proper value of V_B and tuning $e\alpha V_B$ to one of the electrochemical potential levels of the nanoparticle (Figure 1e). Under this condition, the oscillation of α leads to an oscillation of the number of electrons on the nanoparticle, N, between two neighboring ground states characterized by $N = n$ and $N = n + 1$ electrons. The oscillating charge on the nanoparticle causes both a resonance frequency shift, Δf, and damping of the cantilever, $\Delta\gamma$.[7,8] Although tunneling of electrons is a stochastic event, the average charge, $\langle N(t)\rangle$, follows the oscillating motion of the tip. As a result, the oscillating electrostatic force has not only an in-phase, but also a 90° out-of-phase component that leads to energy dissipation (which is a similar effect to the Q-factor degradation in the Q-control system used in amplitude modulation AFM[16]). A detailed quantum mechanical treatment of the coupled cantilever-quantum dot system is needed to understand the experimentally observed frequency and dissipation line shapes, which has been explored in detail elsewhere.[7,8]

We first focus on qualitative observation of the tunneling process by scanning the tip in the area with the three nanoparticles shown in Figure 1d in constant height mode with fixed V_B. Figure 2 shows a set of dissipation (γ) images recorded at a tip height of ≈8 nm (measured from the level of NaCl surface topography characterization) with a fixed bias voltage in the range of 11−13 V. In this situation, although the tip height remains constant (it is only slightly modulated due to the cantilever oscillation amplitude), the level arm α depends on the relative position with respect to the nanoparticle and decreases monotonically as a function of the tip−nanoparticle distance. If the bias voltage is high enough to induce Coulomb oscillations, dissipation features are visible in the γ images as concentric rings centered above nanoparticles. The circular shape is a consequence of the fact that α, to a good approximation, does not depend on the radial direction with respect to a nanoparticle. Considering a single nanoparticle, during the tip scan $e\alpha V_B$ takes its maximal value at closest approach directly above the nanoparticle. If this maximal value matches exactly one of the electrochemical potential levels, which lifts the Coulomb blockade, a disk-like feature will form in the γ image. When the V_B voltage is further increased, the disk transforms into a ring. The width of this disk (and rings) is well understood and depends among other parameters on the oscillation amplitude of the cantilever.[7,8] Each ring originates from a single peak and indicates the spatial positions of the tip where $e\alpha V_B$ is equal to a particular value that lifts the blockade (the largest ring corresponds to the smallest value of $e\alpha V_B$). As shown clearly in Figure 2, the size of the

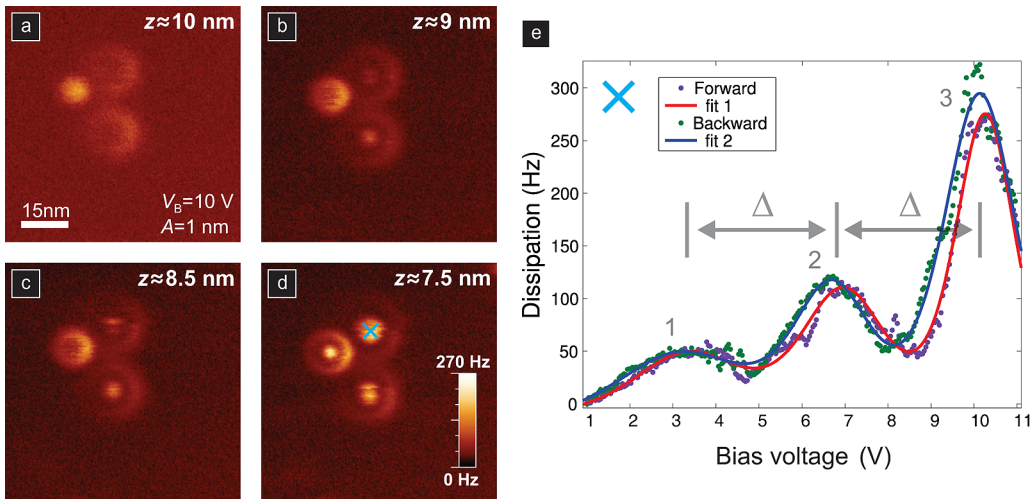

Figure 3. (a–d) Dissipation images showing sequential unloading of electrons from Au nanoparticles through decreasing the tip height, and thus increasing α. (e) γ-V_B spectrum taken at room temperature over the upper nanoparticle with oscillation amplitude A = 1.0 nm and tip height z = 7.5 nm. Similarly to panel (a), where after entering each ring the number of electrons on the nanoparticle reduces by one, the electrons are sequentially unloaded after increasing V_B and passing each peak in the γ-V_B spectrum in panel (e). The level arm, α, is determined by a simultaneous fit describing all three peaks using eq 1. The separation of consecutive peaks, Δ, is given by $E_{add}/e\alpha$, allowing for calculation of nanoparticle addition energy.

nanoparticles is small enough to make the electron addition energy exceed the thermal energy, k_BT, since the rings are clearly resolved at room temperature.

The potential drop across the tunnel barrier can also be controlled by changing the tip height while the bias voltage is kept constant. Decreasing the tip height increases all $\alpha(x,y)$ values and leads to a higher potential drop across the tunnel barrier at all lateral tip positions (x,y). If this change is sufficiently large to access further electrochemical potential levels of the nanoparticle, which are separated by E_{add}, more rings are observed in the γ images. This is demonstrated in Figure 3a–d, where the tip is brought progressively closer to the sample, staring from 10.0 nm and ending up at 7.5 nm, while V_B is fixed at 10 V and the cantilever oscillation amplitude is maintained at 1 nm. Each ring emerges first as a disk above the nanoparticle center and next grows in diameter with decreasing the tip height. As the ring diameter gets larger, the intensity of the ring decreases due to the weaker electrostatic damping force at larger tip-nanoparticle distances.

Figure 3e shows an electron addition spectrum for the upper nanoparticle imaged in Figure 1c (the tip position is also marked with a cross in Figure 3d). The γ-V_B spectrum reveals three distinct peaks which correspond to the concentric rings imaged in Coulomb blockage images in Figures 2 and 3. The dissipation signal is recorded for positive values of V_B, where single electrons sequentially tunnel out of the nanoparticle with increasing V_B (see Figure 1e). If the modulation of $e\alpha V_B$ caused by the cantilever oscillation is smaller than the thermal energy, which is easily met at room temperature, the changes in $\Delta\omega$ and $\Delta\gamma$ are described by a linear response.[8,17,18] In this case, the shape of the Coulomb blockade peak is given by:

$$\Delta\gamma(V_B) = \gamma^0 f(\Delta E)[1 - f(\Delta E)]$$
$$= \gamma^0 \cosh^{-2}\frac{e\alpha(V_B - V^0)}{2k_BT} \quad (1)$$

where $f(\Delta E)$ is the Fermi function evaluated at the point of charge degeneracy, V^0, with $\Delta E = \mu_{NP} - \mu_{BE} = e\alpha(V_B - V^0)$ (μ_{NP} and μ_{BE} are the electrochemical potentials of the nanoparticle and the back electrode, respectively). γ^0 is a constant determined by the measurement temperature, parameters of the cantilever and the coupling strength between the tip and the nanoparticle.[8] In the *e*-EFM method, eq 1 can be used to extract the α parameter without any knowledge about the tip and sample. The solid fitted lines in Figure 3e were obtained by a simultaneous optimization of $\sum_{i=1}^{3}\Delta\gamma_i(\gamma_i^0, V_i^0, \alpha_i)$, yielding on average α = 0.040 (see the Supporting Information for details). Once the α parameter is known, E_{add} can be obtained from the separation of consecutive peaks in the γ-V_B spectrum being $E_{add} = e\alpha\Delta_{i,i+1} = e\alpha(V_{i+1}^0 - V_i^0)$. For the nanoparticle under characterization, the measurement gives the addition energy of $E_{add} = (137 \pm 27)$ meV, confirming $E_{add} \gg k_BT$ requirement. Although in this work we focus on the dissipation signal, a similar addition spectrum was also recorded using the frequency shift, allowing for extraction of tunneling rates, which are within 1 order of magnitude of the resonance frequency of the cantilever (see the Supporting Information).

Before we can relate the measurement of the addition energy to the capacitance of the nanoparticle and draw an equivalent circuit diagram, we perform electrostatic finite element method (FEM) modeling of the studied system using commercially available

COMSOL Multiphysics software (version 4.3a). The considered geometry is depicted in Figure 4a, where the nanoparticle is supported on a 6 ML thick NaCl film (with 5.9 relative permittivity) and its shape is approximated by a solid hemisphere with a radius of 3.5 nm. Above the nanoparticle, at a distance of 8 nm from the NaCl film, there is a metallic tip with a curvature radius of 10 nm (at room temperature heavily doped Si can be approximated by a metal). In total, there are four electrodes: (1) the nanoparticle, (2) the back electrode, (3) the tip, and (4) the system boundary. Figure 4b shows three relevant mutual capacitances in this system. We obtain the following calculated capacitances: $C_{12} = C_{BE} = 2.028$ aF, $C_{13} = C_{TIP} = 0.107$ aF, $C_{14} = C_{ENV} < 0.0002$ aF, and the total capacitance of the hemispherical nanoparticle $C_\Sigma = C_{BE} + C_{TIP} + C_{ENV} = 2.135$ aF. The capacitance between the nanoparticle and the system boundary, *i.e.*, the environment, C_{ENV}, which represents the capacitance to a grounded plane at infinity (often called "self-capacitance"), is negligible. Consequently, the circuit diagram can be reduced to a single electron box, as shown in Figure 4c. In this case, $\alpha = C_{TIP}/C_\Sigma$, and $C_\Sigma = C_{TIP} + C_{BE}$ is the total capacitance of the nanoparticle, where the C_{ENV} component is neglected. The calculated values of the capacitances C_{TIP} and C_{BE} yield $\alpha \approx 0.050$, which is in very good agreement with the value obtained experimentally, although the actual nanoparticle and tip shape may be different. The geometry shown in Figure 4a can also be used to calculate the α parameter by applying a voltage bias, *e.g.*, 1 V, to the tip, grounding the back electrode and keeping the nanoparticle charge-neutral at a floating voltage. Still assuming a hemispherical shape, the calculated voltage at the nanoparticle gives in this situation an indistinguishable value from the previously calculated result using the ratio of capacitances.

Numerical simulation of the hemispherical nanoparticle suggests a very dominant role of C_{BE}, *i.e.*, the mutual capacitance between the nanoparticle and the back electrode in the total capacitance. Most importantly, calculations performed for different tip−sample distances indicate that C_{BE} does not depend strongly on the exact position of the tip that is used in the experiment (see the Supporting Information). An FEM simulation of the capacitance performed for this nanoparticle shape but without the tip leads to a comparable total capacitance of $C_\Sigma = C_{BE} + C_{ENV} = 2.118$ aF. In this case, the capacitance component due to the system boundary is increased, but is still very small $C_{ENV} < 0.007$ aF $\ll C_\Sigma$. We found also that C_{ENV} depends weakly on the size of the system in the 100−1000 nm range used in the FEM modeling. C_{BE} can be still accurately calculated in a geometry that is further simplified by neglecting the tip and assuming $C_\Sigma \approx C_{BE}$. The discrepancy is on the order of C_{TIP}, and since $\alpha = C_{BE}/C_\Sigma$, the percentage discrepancy is approximately equal to α, which in this experiment is about 5%.

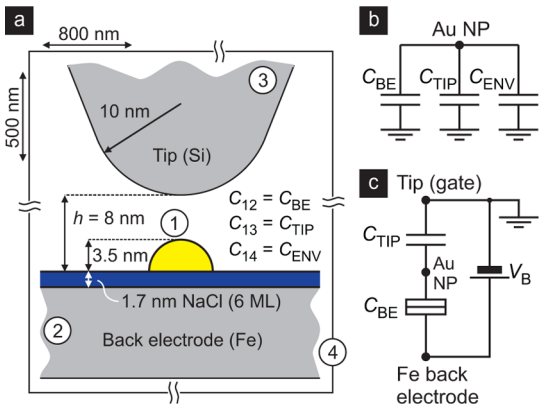

Figure 4. (a) FEM geometry for calculating the capacitance components of the nanoparticle (1). (b) Relevant capacitances to the three electrodes: back electrode (2), tip (3), and system boundary (4). (c) Equivalent circuit diagram for an individual nanoparticle.

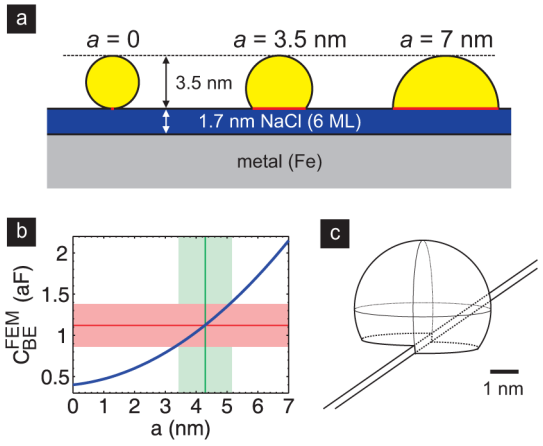

Figure 5. (a) Variously shaped nanoparticles supported on a 6 ML thick NaCl film used in capacitance calculations based on FEM. The shape of truncated spheres of constant height (3.5 nm) is parametrized by *a* describing the diameter of the circular contact area (marked schematically in red). (b) Change in the total capacitance for different *a* parameters showing that the characterized nanoparticle can be best modeled by a truncated sphere with *a* = 4.2 nm leading to $C_{BE}^{FEM} = 1.11$ aF. (c) For a similarly shaped nanoparticle anchored symmetrically above an NaCl step edge (between the sixth and seventh ML), the capacitance is only slightly altered ($C_{BE}^{FEM} = 1.13$ aF).

Given the equivalent circuit diagram of a single electron box, the total capacitance of the nanoparticle can be simply obtained from the experimental value of E_{add} using the relation $E_{add} = e^2/C_\Sigma$, which leads to an experimental (EXP) total capacitance value of $C_\Sigma^{EXP} = (1.16 \pm 0.26)$ aF with $C_{TIP}^{EXP} = (0.046 \pm 0.015)$ aF and $C_{BE}^{EXP} = (1.11 \pm 0.26)$ aF. Clearly, this is much smaller than $C_{BE}^{FEM} \approx 2.14$ aF, *i.e.*, the capacitance calculated for a hemispherical nanoparticle used in the initial approximation above. Increasing the NaCl film thickness from 6 to 7 ML reduces C_{BE}^{FEM} only to 1.95 aF, which does not account for the discrepancy between the experimental and calculated capacitances. What turns out to be highly

relevant, however, is the contact area between the nanoparticle and the back electrode. Because the height of the nanoparticle is precisely known from the experiment (contrary to the lateral size), we can estimate C_{BE}^{FEM} for nanoparticles with different contact areas. We assume a truncated sphere as the shape of the nanoparticles and calculate C_{BE}^{FEM} for different contact areas keeping the same height as shown in Figure 5a. The exact shape is parametrized by only one parameter, a, describing the diameter of the circular contact area between the nanoparticle and the NaCl film. The a parameter can take values from 0 to 7 nm and describe intermediate shapes spanning from a sphere to a hemisphere. The values calculated from the FEM modeling are shown in Figure 5b and indicate a specific shape of the nanoparticle that describes correctly the experimental results. Compared to the hemispherical nanoparticle, the computationally determined truncated sphere has both a smaller radius, $r = (2.4 \pm 0.3)$ nm, and a smaller contact area with a diameter of $a = (4.2 \pm 0.9)$ nm. To take into account the preferential formation of the Au nanoparticles on the step edges on the NaCl film, a corresponding geometry is also modeled (see Figure 5c). For a nanoparticle anchored symmetrically above an NaCl step edge, C_{BE}^{FEM} is only slightly altered and takes a value of 1.13 aF (the radius is fixed at r = 2.4 nm). The determined morphology of the nanoparticle corresponds to a volume of 49 nm^3 containing ≈2900 atoms, and is very similar to the equilibrium shape of Au nano- and microstructures on a weakly interacting graphite surface.[19,20] Interestingly, it also resembles the shape of Au nanoparticles on a more complex, rutile TiO_2(110) surface, which has been characterized experimentally by atomic-resolution scanning transmission electron microscopy[21] and grazing incidence X-ray scattering techniques.[22]

The relatively large number of atoms in the nanoparticle justifies the validity of classical electrodynamics equations used in the FEM calculation, as the number of electrons on the nanoparticle is large enough to consider a continuous distribution of the electrical charge. Similarly, the electron energy level spacing is much smaller than the thermal energy at room temperature, thus corresponding to the classical regime of the Coulomb blockade. In this situation, E_{add} is mostly due to the charging energy of the nanoparticle that is determined by the total capacitance. It is worth mentioning that the self-capacitance of a solid hemisphere with r = 3.5 nm in free space calculated analytically[23] is 0.329 aF. This value is significantly larger than the C_{ENV} component (C_{ENV} < 0.0002 aF) calculated above where the hemispherical nanoparticle is supported on an NaCl film. This clearly suggests that the concept of self-capacitance defined as the capacitance with reference to a grounded plane at infinity cannot be used to estimate the total capacitance of the system with nanoparticles coupled to nearby electrodes. It should be noted that the effect of the self-capacitance on single-electron charging has not been sufficiently emphasized in the literature, and its subtle aspects were only discussed by Ohgi *et al.*[24] Especially, we found that the total capacitance cannot be divided into a fixed self-capacitance component, which is given by the shape of the nanoparticle, and mutual capacitances to the electrodes. Even though this can be still conceptually done, such defined capacitances are not additive and do not sum up to the total capacitance of the nanoparticle. This observation has a fundamental impact on the design of nanoelectronic circuits, where the components have to meet desired requirements for capacitances that determine coupling and charging effects. For instance, in our study the total capacitance of the nanoparticle is dominated by the mutual capacitance to the back electrode, which can be primarily controlled by adjusting the contact area between the nanoparticle and the dielectric film.

Given the fabrication flexibility and the fact that all measurements were performed *in situ* on samples prepared under ultraclean conditions, the presented method can be easily extended to other areas. The well-defined morphology makes the system approachable by various theoretical methods, including density functional theory and molecular dynamics. A variety of nanoscale processes on alkali halide surfaces have been well characterized, such as the self-assembly of metal clusters and large organic molecules.[25] Such detailed understanding makes the fabricated system attractive for further studies. For instance, organic molecules can be used to interconnect two Au nanoparticles[26,27] and control their mutual capacitance and quantum mechanical interactions. In this way, coherent tunneling in coupled quantum dots[28] could be systematically studied *in situ*. Our approach is also applicable to studies of model catalysis on various insulating oxide films at temperatures as high as room temperature, as there is a close analogy with the widely studied system of Au nanoparticles supported on MgO films.[29] Au nanoparticles are known to be a very efficient catalyst that can be active over a wide range of temperatures.[30] The chemical functionality of such metal nanostructures depends crucially on their size and shape, as well as the charge state,[31] which can be characterized by *e*-EFM. The size of nanoparticles used in this study is very close to the regime in which Au reveals maximal chemical activity.[31] By shortening the evaporation time this size can be reduced leading to enhanced electronic quantum size effects that play a significant role in oxidation of CO molecules by Au nanoclusters.[32] The *e*-EFM method could be used not only to sense the charge state of individual Au clusters, but also to resolve electronic quantum energy levels and observe changes in frontier orbitals upon interaction with reactants.

CONCLUSIONS

We have demonstrated that by exercising precise control over sample design and growth the *e*-EFM technique can be used to characterize single-electron charging at room temperature. The electron addition

energy of a 3.5 nm tall Au nanoparticle supported on a 6 ML thick NaCl film is measured as $E_{add} = (137 \pm 27)$ meV, which substantially exceeds the thermal energy and allows for observation of the Coulomb blockade at room temperature. Electrostatic FEM calculations indicate that the total nanoparticle capacitance is dominated by the mutual capacitance to the back electrode. The nanoparticle shape modeled that best matched our experimental data was a truncated sphere, in which the mutual capacitance to the substrate can be reduced. Flexible *in situ* fabrication based on well-characterized UHV processing techniques of alkali halide surfaces can extend the *e*-EFM technique to room temperature characterization of other systems on thin insulating films. In particular, this approach can be used to study quantum mechanically coupled quantum dots and the catalytic activity of Au nanoclusters at room temperature.

METHODS

The experiment, including sample preparation and characterization, was performed in a modified commercial JEOL JSPM 4500a UHV AFM system. The detailed preparation procedure of the NaCl film, which was grown on an Fe(001)-p(1 × 1)O surface, is described elsewhere.[11] A submonolayer of Au was deposited by an electron-beam evaporator (Oxford Applied Research EGN4, fitted with a charge-retarding grid) onto the sample kept at room temperature. For data acquisition and cantilever oscillation, a scanning probe microscope (SPM) control system from SPECS-Nanonis was used. A highly doped Si cantilever (Nanosensors PPP-QNCHR) with a resonance frequency of approximately 286 kHz, *Q*-factor of 33 000 and nominal spring constant of 42 N/m was oscillated with a phase-locked loop oscillation controller (OC4 from Nanonis). The amplitude controller was used to regulate the driving signal amplitude in order to keep the oscillation amplitude constant while tracking the resonance frequency of the cantilever with a phase-locked loop. The topography images were taken in constant frequency shift mode, where the frequency shift of the cantilever was maintained constant by the SPM feedback loop controlling the *z*-piezo position. The dissipation of the cantilever can be extracted by measuring the *Q*-factor degradation, which corresponds to the amplitude of the cantilever drive signal needed to keep the amplitude of the oscillation constant.[8] The dissipation images were recorded in constant-height mode with linear *z*-drift compensation.[33] The correction for the vertical drift improved the stability of the tip height at room temperature by reducing its change to only a fraction of a nanometer over the time needed to scan one frame, which typically was 15 min. During the experiment, the vacuum pressure was maintained in the low 10^{-8} Pa range.

Conflict of Interest: The authors declare no competing financial interest.

Acknowledgment. We acknowledge helpful discussions with Antoine Roy-Gobeil from McGill University. This work was partly supported by Natural Sciences and Engineering Research Council (NSERC), Canadian Institute for Advanced Research (CIfAR), Canadian Microelectronics Corporation (CMC) and Regroupement Québécois sur les Matériaux de Pointe (RQMP). A.T. gratefully acknowledges NSERC for financial support as a Vanier Canada Graduate Scholar.

Supporting Information Available: Additional details about the *e*-EFM method, best-fit parameters, estimation of tunneling rates and finite element electrostatic simulations. This material is available free of charge *via* the Internet at http://pubs.acs.org.

REFERENCES AND NOTES

1. Likharev, K. Single-Electron Devices and Their Applications. *Proc. IEEE* **1999**, *87*, 606–632.
2. Ray, V.; Subramanian, R.; Bhadrachalam, P.; Ma, L.-C.; Kim, C.-U.; Koh, S. J. CMOS-Compatible Fabrication of Room-Temperature Single-Electron Devices. *Nat. Nanotechnol.* **2008**, *3*, 603–608.
3. Woodside, M. T.; McEuen, P. L. Scanned Probe Imaging of Single-Electron Charge States in Nanotube Quantum Dots. *Science* **2002**, *296*, 1098–1101.
4. Zhu, J.; Brink, M.; McEuen, P. L. Frequency Shift Imaging of Quantum Dots with Single-Electron Resolution. *Appl. Phys. Lett.* **2005**, *87*, 242102.
5. Stomp, R.; Miyahara, Y.; Schaer, S.; Sun, Q.; Guo, H.; Grutter, P.; Studenikin, S.; Poole, P.; Sachrajda, A. Detection of Single-Electron Charging in an Individual InAs Quantum Dot by Noncontact Atomic-Force Microscopy. *Phys. Rev. Lett.* **2005**, *94*, 056802.
6. Zhu, J.; Brink, M.; McEuen, P. L. Single-Electron Force Readout of Nanoparticle Electrometers Attached to Carbon Nanotubes. *Nano Lett.* **2008**, *8*, 2399–2404.
7. Bennett, S. D.; Cockins, L.; Miyahara, Y.; Grütter, P.; Clerk, A. A. Strong Electromechanical Coupling of an Atomic Force Microscope Cantilever to a Quantum Dot. *Phys. Rev. Lett.* **2010**, *104*, 017203.
8. Cockins, L.; Miyahara, Y.; Bennett, S. D.; Clerk, A. A.; Studenikin, S.; Poole, P.; Sachrajda, A.; Grutter, P. Energy Levels of Few-Electron Quantum Dots Imaged and Characterized by Atomic Force Microscopy. *Proc. Natl. Acad. Sci. U.S.A.* **2010**, *107*, 9496–9501.
9. Cockins, L.; Miyahara, Y.; Bennett, S. D.; Clerk, A. A.; Grutter, P. Excited-State Spectroscopy on an Individual Quantum Dot Using Atomic Force Microscopy. *Nano Lett.* **2012**, *12*, 709–713.
10. Hattori, S.; Kano, S.; Azuma, Y.; Tanaka, D.; Sakamoto, M.; Teranishi, T.; Majima, Y. Coulomb Blockade Behaviors in Individual Au Nanoparticles as Observed Through Noncontact Atomic Force Spectroscopy at Room Temperature. *Nanotechnology* **2012**, *23*, 185704.
11. Tekiel, A.; Topple, J.; Miyahara, Y.; Grütter, P. Layer-by-Layer Growth of Sodium Chloride Overlayers on an Fe(001)-p(1 × 1)O Surface. *Nanotechnology* **2012**, *23*, 505602.
12. Barth, C.; Henry, C. R. High-Resolution Imaging of Gold Clusters on KBr(001) Surfaces Investigated by Dynamic Scanning Force Microscopy. *Nanotechnology* **2004**, *15*, 1264–1272.
13. Pakarinen, O.; Barth, C.; Foster, A.; Nieminen, R.; Henry, C. High-Resolution Scanning Force Microscopy of Gold Nanoclusters on the KBr(001) Surface. *Phys. Rev. B* **2006**, *73*, 235428.
14. Barth, C.; Henry, C. R. Gold Nanoclusters on Alkali Halide Surfaces: Charging and Tunneling. *Appl. Phys. Lett.* **2006**, *89*, 252119.
15. Barth, C.; Pakarinen, O. H.; Foster, A. S.; Henry, C. R. Imaging Nanoclusters in the Constant Height Mode of the Dynamic SFM. *Nanotechnology* **2006**, *17*, S128–S136.
16. Sulchek, T.; Hsieh, R.; Adams, J. D.; Yaralioglu, G. G.; Minne, S. C.; Quate, C. F.; Cleveland, J. P.; Atalar, A.; Adderton, D. M. High-Speed Tapping Mode Imaging with Active Q Control for Atomic Force Microscopy. *Appl. Phys. Lett.* **2000**, *76*, 1473–1475.
17. Clerk, A. Quantum-Limited Position Detection and Amplification: A Linear Response Perspective. *Phys. Rev. B* **2004**, *70*, 245306.
18. Clerk, A. A.; Bennett, S. Quantum Nanoelectromechanics with Electrons, Quasi-Particles and Cooper Pairs: Effective Bath Descriptions and Strong Feedback Effects. *New J. Phys.* **2005**, *7*, 238.
19. Heyraud, J.; Métois, J. Establishment of the Equilibrium Shape of Metal Crystallites on a Foreign Substrate: Gold on Graphite. *J. Cryst. Growth* **1980**, *50*, 571–574.

20. Guerra, R.; Tartaglino, U.; Vanossi, A.; Tosatti, E. Ballistic Nanofriction. *Nat. Mater.* **2010**, *9*, 634–637.
21. Sivaramakrishnan, S.; Wen, J.; Scarpelli, M.; Pierce, B.; Zuo, J.-M. Equilibrium Shapes and Triple Line Energy of Epitaxial Gold Nanocrystals Supported on TiO_2(110). *Phys. Rev. B* **2010**, *82*, 195421.
22. Lazzari, R.; Renaud, G.; Jupille, J.; Leroy, F. Self-Similarity During Growth of the Au/TiO_2(110) Model Catalyst as Seen by the Scattering of X-Rays at Grazing-Angle Incidence. *Phys. Rev. B* **2007**, *76*, 125412.
23. Lebedev, N. N.; Skalskaya, I. P.; Uflyand, Y. S. *Worked Problems in Applied Mathematics*; Dover Publications: New York, 1979.
24. Ohgi, T.; Fujita, D. Consistent Size Dependency of Core-Level Binding Energy Shifts and Single-Electron Tunneling Effects in Supported Gold Nanoclusters. *Phys. Rev. B* **2002**, *66*, 115410.
25. Gnecco, E.; Szymonski, M. *Nanoscale Processes on Insulating Surfaces*; World Scientific Publishing Co. Pte. Ltd.: Singapore, 2009.
26. Mativetsky, J. M.; Burke, S. A.; Fostner, S.; Grutter, P. Nanoscale Pits as Templates for Building a Molecular Device. *Small* **2007**, *3*, 818–821.
27. Topple, J. M.; Burke, S. A.; Ji, W.; Fostner, S.; Tekiel, A.; Grutter, P. Tailoring the Morphology and Dewetting of an Organic Thin Film. *J. Phys. Chem. C* **2011**, *115*, 217–224.
28. Gardner, J.; Bennett, S. D.; Clerk, A. A. Mechanically Probing Coherent Tunneling in a Double Quantum Dot. *Phys. Rev. B* **2011**, *84*, 205316.
29. Pacchioni, G., Valeri, S., Eds. *Oxide Ultrathin Films*; Wiley-VCH Verlag GmbH & Co. KGaA: Weinheim, Germany, 2011.
30. Daniel, M.-C.; Astruc, D. Gold Nanoparticles: Assembly, Supramolecular Chemistry, Quantum-Size-Related Properties, and Applications toward Biology, Catalysis, and Nanotechnology. *Chem. Rev.* **2004**, *104*, 293–346.
31. Choudhary, T.; Goodman, D. Catalytically Active Gold: The Role of Cluster Morphology. *Appl. Catal., A* **2005**, *291*, 32–36.
32. Lopez-Acevedo, O.; Kacprzak, K. A.; Akola, J.; Häkkinen, H. Quantum Size Effects in Ambient CO Oxidation Catalysed by Ligand-Protected Gold Clusters. *Nat. Chem.* **2010**, *2*, 329–334.
33. Abe, M.; Sugimoto, Y.; Namikawa, T.; Morita, K.; Oyabu, N.; Morita, S. Drift-Compensated Data Acquisition Performed at Room Temperature with Frequency Modulation Atomic Force Microscopy. *Appl. Phys. Lett.* **2007**, *90*, 203103.